PCCP

Narrowing the Band Gap and Suppressing Electron–Hole Recombination in β-Fe2O3 by Chlorine Doping

Journal:	*Physical Chemistry Chemical Physics*
Manuscript ID	CP-ART-10-2022-004723.R1
Article Type:	Paper
Date Submitted by the Author:	30-Dec-2022
Complete List of Authors:	He, Gaoxiang; Nanjing University Lu, Linguo; University of Puerto Rico, Department of Chemistry Zhang, Ningsi; Nanjing University Liu, Wangxi; Nanjing University Chen, Zhongfang; University of Puerto Rico, Chemistry Li, Zhaosheng; Nanjing University, Materials Science and Engineering Zou, Zhigang; Nanjing University, Physics

PCCP

ARTICLE

Received 00th January 20xx,
Accepted 00th January 20xx

DOI: 10.1039/x0xx00000x

Narrowing the Band Gap and Suppressing Electron–Hole Recombination in β-Fe_2O_3 by Chlorine Doping

Gaoxiang He[a], Linguo Lu[b], Ningsi Zhang[a], Wangxi Liu[a], Zhongfang Chen*[b], Zhaosheng Li*[a], Zhigang Zou[a]

The effects of halogen (F, Cl, Br, I, and At) doping in the direct-band-gap β-Fe_2O_3 semiconductor on its band structures and electron–hole recombination have been investigated by density functional theory. Doping Br, I, and At in β-Fe_2O_3 leads to transformation from a direct-band-gap semiconductor to an indirect-band-gap semiconductor because their atomic radii are too large; however, F- and Cl-doped β-Fe_2O_3 remain as direct-band-gap semiconductors. Due to the deep impurity states of the F dopant, this study focuses on the effects of the Cl dopant on the band structures of β-Fe_2O_3. Two impurity levels are introduced when Cl is doped into β-Fe_2O_3, which narrows the band gap by approximately 0.3 eV. After doping Cl, the light-absorption edge of β-Fe_2O_3 redshifts from 650 to 776 nm, indicating that its theoretical solar to hydrogen efficiency for solar water splitting increases from 20.6% to 31.4%. In addition, the effective mass of the holes in halogen-doped β-Fe_2O_3 becomes significantly larger than that in undoped β-Fe_2O_3, which may suppress electron–hole recombination.

Introduction

With the rapid development of industrialization, extensive exploitation of fossil fuels has resulted in excessive greenhouse gas emissions.[1, 2] To achieve the goal of carbon neutrality, there is an urgent need to develop technologies to produce renewable and green energy.[3-5] One promising strategy is to use inexhaustible solar energy to produce hydrogen by photoelectrochemical (PEC) or photocatalytic water splitting.[6-11] Therefore, it is imperative to develop visible-light-responsive, environmentally friendly, low-cost, and robust semiconductors to realize efficient PEC or photocatalytic water splitting.[12-14]

Great achievements have been made in developing visible-light-responsive semiconductor photocatalysts, such as $BiVO_4$, Ta_3N_5, WO_3, $SrTaO_2N$, and α-Fe_2O_3.[15-19] Recently, as an isomer of α-Fe_2O_3, the metastable β-Fe_2O_3 semiconductor has emerged as a promising photocatalyst for solar water splitting owing to its direct band gap of 1.9 eV and wide spectral response range (≤650 nm).[20] The theoretical solar-to-hydrogen (STH) efficiency of the β-Fe_2O_3 semiconductor for solar water splitting is 20.6%. However, the poor electrical conductivity and severe electron–hole recombination of β-Fe_2O_3 photoanodes hinder their PEC water-splitting performance. To overcome these disadvantages, cation doping, such as Zr and Ti doping, has been used to improve the conductivity and reduce the charge recombination of β-Fe_2O_3. Still, the Zr and Ti dopants do not significantly affect the band gap and light-absorption ability of β-Fe_2O_3[21, 22]. In comparison, the effects of anion doping on the band structure of β-Fe_2O_3 have not been explored to our best knowledge.

Here, we investigated the effect of halogen (F, Cl, Br, I, and At) doping of β-Fe_2O_3 by density functional theory (DFT) computations. The effects of both dopant types and doping concentrations on the band gap were studied, and the effective masses of electrons and holes were also calculated. Our results suggest that Cl doping in β-Fe_2O_3 can narrow its band gap, suppress electron–hole recombination, and thus significantly improve the photocatalytic performance for water splitting.

Computational Method

Computational details

The DFT calculations were performed with the Vienna Ab initio Software Package.[23] The generalized gradient approximation (GGA) was used for the exchange–correlation potential.[24] The Perdew–Burke–Ernzerhof (PBE)[25] density functional was used to describe the core and valence electrons. After a series of tests, the plane-wave cut-off energy of 500 eV was used to achieve reasonable convergence. Geometries were optimized until energy and force convergence were less than 10^{-5} eV and 0.02 eV/Å, respectively. Considering that β-Fe_2O_3 is

[a] Collaborative Innovation Center of Advanced Microstructures, National Laboratory of Solid State Microstructures and School of Physics, Nanjing University, 22 Hankou Road, Nanjing 210093, People's Republic of China. E-mail: zsli@nju.edu.cn
[b] Department of Physics, University of Puerto Rico, Rio Piedras Campus, San Juan, PR 00931, USA.
† Electronic Supplementary Information (ESI) available:. See DOI:

strongly correlated with the electron system, the GGA+U method was used to remedy the effect derived from localized d electrons, for which the effective on-site Coulomb interaction parameter of Fe was chosen as 5.3.[26, 27] Brillouin zone integration of β-Fe_2O_3 was performed with 7×7×7 *k*-point meshes.[28]

Crystal structure

β-Fe_2O_3 is a transition-metal oxide with point group $m\bar{3}$ and space group $Ia\bar{3}$.[29] In this study, the conventional standard cell is used, which contains 32 Fe and 48 O atoms with $a = b = c =$ 9.556 Å. Each angle between the two base vectors of the unit cell is 90°. The metal site at the top makes up the tetrahedron, and each O atom is at the center of the tetrahedron. We doped halogen family elements into β-Fe_2O_3. The halogen element replaces the O site at the center of the tetrahedron in β-Fe_2O_3.

Formation energy

The defect-formation energy ($E^{\mathrm{f}}_{\mathrm{defect}}(\mathrm{X_O})$) is used as the descriptor to evaluate the structure's stabilities and is calculated as follows:[30]

$$E^{\mathrm{f}}_{\mathrm{defect}}(\mathrm{X_O}) = E^{\mathrm{t}}_{\mathrm{defect}}(\mathrm{X_O}) - E^{\mathrm{t}}_{\mathrm{bulk}} + \sum_i n_i\mu_i$$

where X represents the doping elements (X = O, F, Cl, Br, I, or At); i represents the atom to be replaced (i = X); $E^{\mathrm{t}}_{\mathrm{defect}}(\mathrm{X_O})$ and $E^{\mathrm{t}}_{\mathrm{bulk}}$ are the total energies of the structures with and without defects, respectively; n_i is the number of defects; and μ_i is the chemical potential of the i atom. When the i atom is moved from the vacuum to the conventional cell, n_i is negative; in contrast, when the i atom is transferred from the conventional cell to the vacuum, n_i is positive. By the above definition, a smaller defect-formation energy indicates a more stable lattice structure.

Calculation of solar-to-hydrogen efficiency

The solar-to-hydrogen efficiency (STH) for a PEC system can be calculated by the following equations.

$$\mathrm{STH} = \frac{J_{\mathrm{p}} \times 1.229}{I_0} \times 100\%$$

$$J_{\mathrm{p}} = q\int_0^{1240/E_g} \mathrm{IPCE}(\lambda)N(\lambda)\mathrm{d}\lambda$$

In theoretical calculations, the incident photon-to-electron conversion efficiency (IPCE) should be 100%. $N(\lambda)$ represents the incident photon flux set to wavelength λ. q is applied to describe the charges of electrons. I_0 is the light intensity of solar illumination. E_g is the band gap of a semiconductor.[31]

Results and discussion

Structure optimization

The optimized structure of pure β-Fe_2O_3 is shown in Fig. 1a. The equilibrium lattice parameters ($a = b = c =$ 9.546 Å) are in good agreement with the experimental data ($a = b = c =$ 9.393 Å),[32] with deviations of less than 1.7% in the structural parameters. Each halogen atom doped into the unit cell replaced an O atom at the center of a tetrahedron, as shown in Figs. 1b–g and S1. The atom numbers in the CONTCAR file were used to label the different Fe atoms (Fe6, Fe14, Fe19, and Fe28). The defect-formation energies for halogen atoms with different radii are summarized in Fig. S2. The lattice parameters and bond length between doping sites and surrounding Fe increase with increasing radius of halogen atoms, as shown in Fig. 1h and 1i. In addition, for all the halogen dopants, the doping site with Fe28 has the shortest interbond length, which may cause strongly directed electronic property control.

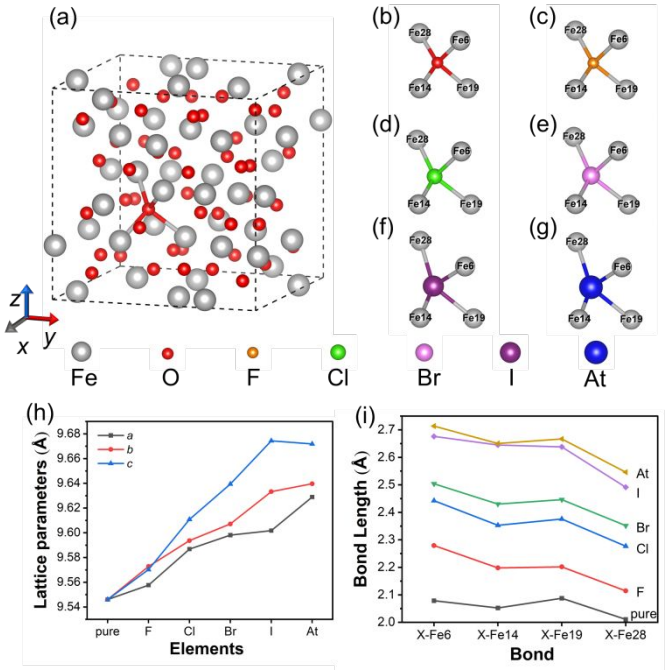

Fig. 1 (a) Optimized geometric structure of pure β-Fe_2O_3. The Fe atoms surrounding an O atom form a tetrahedron, as shown by the bonds (sticks) between an O atom and four Fe atoms. (b)–(g) Tetrahedra of the pure and halogen-doped β-Fe_2O_3 structures after geometry optimizations. (h) Lattice parameters of the optimized pure and halogen-doped β-Fe_2O_3. (i) Bond lengths between the X and Fe atoms (X = O (pure), F, Cl, Br, I, and At).

Band structure and density of states

To explore the electronic properties, we calculated the band structures of the halogen-doped β-Fe_2O_3 systems (Fig. S3; the details about the *k*-point path[33] (Γ–H–N–Γ–P–H) are given in Fig. S4 and Table S2).

The atomic substitution by an element with a larger size will introduce deep energy states that can act as centers for the recombination of carriers,[34] and the pure and Cl-doped β-Fe_2O_3 will be investigated in detail. Furthermore, Br, I, and At in β-Fe_2O_3 leads to transformation from a direct-band-gap semiconductor to an indirect-band-gap semiconductor because of their atomic radii are too large, thus will not be discussed in detail.

Pure β-Fe_2O_3 is a direct semiconductor with a band gap of 1.4 eV at the PBE level of theory (Fig. 2a).[21] Even though the PBE functional underestimates the band gap value (compared with the experimental value of 1.9 eV) as expected, it can still predict the variation tendency and provide some details of the band structure

change.[35] The difference between the calculation and experiment is because the Hartree–Fock exchange energy is not considered

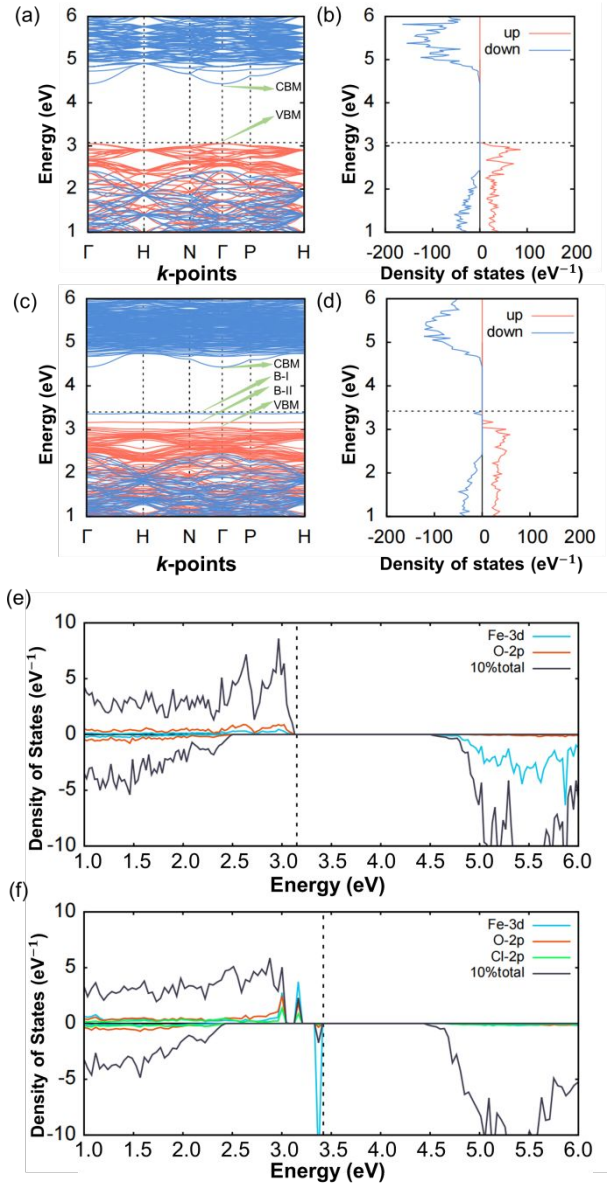

Fig. 2 (a) Band structure of pure β-Fe_2O_3. (b) Electronic density of states of pure β-Fe_2O_3. (c) Band structure of Cl-doped β-Fe_2O_3. (d) Electronic density of states of Cl-doped β-Fe_2O_3. (e) Electronic partial density of states of pure β-Fe_2O_3. (f) Electronic density of states of Cl-doped β-Fe_2O_3.

in the PBE functional.[36-38] At the H point in Fig. 2a, the band structure possesses high degeneracy due to its high symmetry.

However, heteroatom doping breaks the high symmetry of the pure β-Fe_2O_3, and eliminates the band degeneracy, especially at the H point. The symmetry breaking is mainly from the change in atomic radii and electronegativities. Note that the symmetry breaking observed here is consistent with previous DFT calculations of BiOBr by Guo et al.[39] Along with degeneracy elimination, the curvature of the valance-band maximum (VBM) becomes flatter, leading to a larger effective mass and enhanced electron localization.

Cl doping introduces two impurity levels (Fig. 2c and d), similar to the F- and Cl-doped anatase TiO_2.[40, 41] One impurity level is located at the Fermi level, which is marked as impurity band I (B-I). In other words, the Fermi level is raised owing to the introduction of this impurity level. The other impurity level is located between the Fermi level and VBM, denoted as impurity band II (B-II). As carrier donors, the gap between the impurity levels and conduction-band minimum (CBM) is significantly smaller than that between the VBM and CBM.

To identify the influence of doping atoms on the coordinated Fe, we compared the partial density of states (PDOS) of the pure and Cl-doped β-Fe_2O_3 (Fig. 2e and 2f).

Upon doping, one new peak (B-I), mainly contributed by Fe 3d, appears at approximately 3.4 eV. This indicates that the excess electron of the Cl atom (relative to the O atom) is transferred to the Fe28 atom (Cl has seven valence electrons, while O has six valence electrons). In the pure β-Fe_2O_3 (Fig. 2e), there exists the Fe 3d unoccupied conductive band above 4.54 eV; however, this band disappears in the C-doped system, instead, a new peak appears around the Fermi level (3.30 to 3.37 eV, Fig. 2f). The shift of the Fe 3d band from above 4.54 eV in the pure β-Fe_2O_3 to the Fermi level in the C-doped system can be easily understood: the redundant electron quickly occupies the unoccupied Fe 3d conductive band, as shown by the band-decomposed charge densities (Fig. 3b).

The peak from 3.16 to 3.18 represents B-II (Fig. 2f), composed of Fe 3d, O 2p, and Cl 2p orbitals. Clearly, in the Cl-doped system, Cl replaces the position of O to form some bonding with Fe, and the Fe 3d orbital combines with both the O 2p and Cl 2p orbitals, while the bonding of Fe-Cl does not exist in the pure β-Fe_2O_3. Because the Cl atom has smaller electronegativity than the O atom, more electrons transfer from the Cl 2p orbital to the Fe 3d orbital. Consequently, the density of states of the Cl 2p orbital is significantly lower than that of the Fe 3d orbital and slightly lower than that of the O 2p orbital. The introduction of halogen atoms brings some covalent bond character to the otherwise pure ionic bonds in the pristine β-Fe_2O_3. Such a phenomenon was also observed in Cl-doped TiO_2.[40]

Band-decomposed charge densities

To better understand the impurity bands, we calculated the band-decomposed charge densities of these bands to examine the charge-density distribution in real space.

As shown in Fig. 3a, most electrons of B-I are distributed between Fe28 and its adjacent O atoms, while some are between Fe28 and Cl. For B-II, there is no electron cloud between Fe and Cl, which suggests that all the excess electrons transfer from Cl to the Fe28 atom. The bonding electron and excess electron are always located at Fe28 (Fig. 3a and b), indicating strong directivity of the Cl–Fe bond. Note that Galli and coworkers derived similar results for excess electrons near defects.[42]

The band-decomposed charge densities of B-I and B-II bands around the VBM were also studied (Fig. 3c). The dashed line pointing to the Fe28 atom represents the direction of the charge density of the O atom. The bonding between the Fe28 and O atoms is the strongest, and such bonding leads to a shorter bond

length (Fig. 1i). Because the Fe–Cl bond replaces the Fe–O bond, the character of the Fe–Cl bond is similar to that of the Fe–O bond. Consequently, the length of the Fe28–Cl bond is shorter than the other three Fe–Cl bonds, and electrons prefer to locate at Fe28 rather than the other Fe atoms.

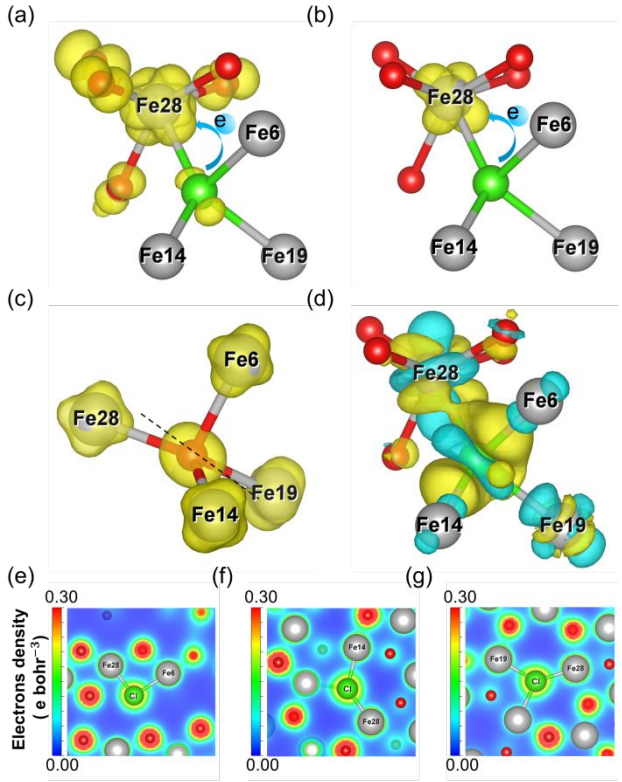

Fig. 3 (a) Electron distribution of B-II with an isosurface level of 0.005 e bohr^{-3}. (b) Electron distribution of B-I with an isosurface level of 0.015 e bohr^{-3}. (c) Sum of all of the bands around energies of 2.65 and 3.02 eV of pure β-Fe_2O_3 with an isosurface level of 0.01 e bohr^{-3}. (d) Differential charge of Cl-doped β-Fe_2O_3 with an isosurface level of 0.005 e bohr^{-3}. The yellow region represents an increase in the number of electrons, and the blue region represents a decrease in the number of electrons. (e)–(f) Charge-density contour plots in the planes for selected atoms, (Fe28, Cl, Fe6); (Fe28, Cl, Fe6) and (Fe28, Cl, Fe6), respectively.

Electron density

We further investigated the interaction between the Cl and Fe atoms by calculating the charge-density difference (Fig. 3d). The electrons tend to accumulate in the vacuum area between the Fe atom and Cl atom and in the area around the Fe28 atom. To better understand the chemical bonding, we examined the charge-density contour plots in the planes for selected atoms (Fig. 3e–g, respectively). Electrons accumulate around the Cl atom rather than at the core of the atom. Both the charge-density difference and the charge-density contour plots indicate that the Cl–Fe bond tends to possess more covalent character than the O–Fe bonds.

The effective Bader charge[43] is defined as $q = Z_{\mathrm{val}} - q_{\mathrm{Bader}}$, where Z_{val} is the number of valence electrons and q_{Bader} is the calculated Bader charge. To provide deeper insight into the charge transfer at the atomic level, we calculated the effective Bader charges of Fe, O, and Cl in β-Fe_2O_3 and Cl-doped β-Fe_2O_3 by Bader charge analysis (Table 1).[44, 45] The valence electrons are Cl $^{3\ s2p5}$, O $^{2\ s2p4}$, and Fe $3p^6d^64s^2$. The results show that for pure β-Fe_2O_3, the Fe and O atoms have effective Bader charges of +1.85 e and −1.23 e, respectively. For Cl-doped β-Fe_2O_3, the Fe6, Fe14, and Fe19 atoms have effective Bader charges of +1.80 e, +1.79 e, and +1.78 e, respectively. The effective Bader charges of Fe6, Fe14, and Fe19 in Cl-doped β-Fe_2O_3 are less than those in pure β-Fe_2O_3 because the electronegativity of Cl is lower than that of O. The effective Bader charge of Fe28 is +1.37 e, which is significantly less than those of Fe6, Fe14, and Fe19. This is because the bond length between Fe28 and Cl is the shortest, and Fe28 can attract more electrons. The Cl atom has an effective Bader charge of −0.60 e. Compared with the effective Bader charge of O of −1.23 e, Cl has 0.63 fewer electrons, which can be understood by its lower electronegativity and the fact that part of the redundant electron being attracted by Fe28.

Table 1 Effective Bader charges (q) of pure and Cl-doped β-Fe_2O_3.

	Fe6	Fe14	Fe19	Fe28	O	Cl
pure	+1.85	+1.85	+1.85	+1.85	−1.23	
Cl-doped	+1.80	+1.79	+1.78	+1.37		−0.60

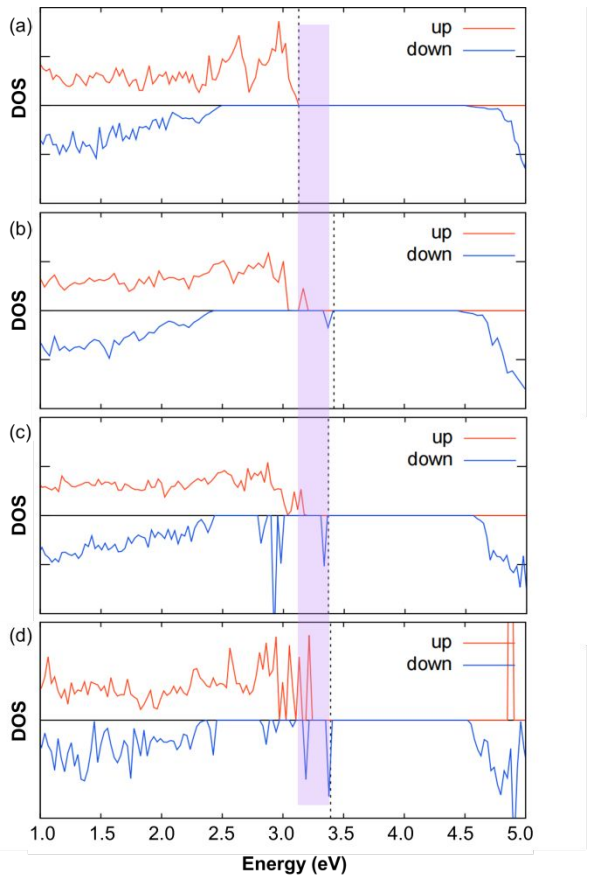

Fig. 4 DOS diagrams of (a) pure, (b) 1.25% Cl-doped, (c) 2.50% Cl-doped, and (d) 3.75% Cl-doped β-Fe_2O_3. The density in the purple area increases with increasing Cl concentration.

Effect of the Cl doping concentration

The above results show that the introduction of impurity bands can remarkably reduce the band gap and improve the light-absorption ability. However, the low density below the Fermi level may limit the photoexcited rate of electrons. Therefore, to increase the density of the impurity bands, we investigated different doping concentrations of Cl (1.25%, 2.50% and 3.75%) (Fig. S7).

Fig. 4 summarizes the density of states of undoped, 1.25% Cl-doped, 2.50% Cl-doped, and 3.75% Cl-doped β-Fe_2O_3. In the purple area, the density of states remarkably increases with increasing Cl concentration, suggesting improved effective electrons during photocatalysis. The interval between B-II and the valence band disappears, which causes an increase in the valence band. The energy gap of pure β-Fe_2O_3 is 1.4 eV, whereas the energy gap of 3.75% Cl-doped β-Fe_2O_3 is 1.1 eV, which means that the band gap narrows by approximately 0.3 eV at such a high doping concentration. Considering that the β-Fe_2O_3 semiconductor has a band gap of 1.9 eV and spectral response range (≤650 nm), we can estimate that the actual 3.75% Cl-doped β-Fe_2O_3 has a band gap of 1.6 eV, the absorption edge increases from 650 to 776 nm, and the theoretical STH efficiency for solar water splitting increases from 20.6% for undoped β-Fe_2O_3 to 31.4% for Cl-doped β-Fe_2O_3.[31]

Effective carrier mass

Fast carrier migration and reduced combination of electrons and holes are beneficial to the performance of a photocatalyst. Since carriers with smaller effective mass have higher mobilities, we calculated the effective mass of electrons and holes for both the pure and Cl-doped β-Fe_2O_3 (doping concentration of 1.25%). For pure β-Fe_2O_3, the effective carrier masses in the VBM and CBM were examined (Table 2); while for the Cl-doped β-Fe_2O_3, we studied the effective masses of holes and electrons in the VBM, B-I, B-II, and CBM (Table 3).

Table 2 Effective masses of carriers in pure β-Fe_2O_3.

		Γ-H	Γ-N	Γ-P
holes	VBM	−5.97	−6.17	−5.78
electrons	CBM	1.68	1.69	1.59

Table 3 Effective masses of carriers in 1.25% Cl-doped β-Fe_2O_3

		Γ-H	Γ-N	Γ-P
holes	VBM	−7.83	−7.93	−4.35
	B-II	20.03	−38.73	−63.16
	B-I	−48.50	28.95	45.48
electrons	CBM	1.79	1.79	1.73

Comparing the VBMs of the pure and the Cl-doped β-Fe_2O_3, the effective mass at the Γ point moderately increases after Cl doping. This increase is derived from the combined action of distortion of the lattice parameters and the formation of the Fe–Cl bond. The B-I and B-II in Cl-doped β-Fe_2O_3 are significantly flatter than the VBM in the pure β-Fe_2O_3. The effective masses of B-I and B-II in Cl-doped β-Fe_2O_3 are 4 to 10 times larger than those of the VBM in pure β-Fe_2O_3, indicating strong localization in these two impurity states, which can remarkably reduce electron–hole recombination. In addition, the change in the effective mass in the CBM is small.

The suppression of recombination is described by the quotient of the hole effective mass divided by the electron effective mass. The relative ratio of the effective mass D is defined by[46, 47]

$$D = \left|\frac{m_h^*}{m_e^*}\right|$$

A higher D value indicates stronger suppression of recombination. The relative ratios in the VBM, B-I, and B-II are given in Table 4. The $D_{V/C}$ in the Cl-doped β-Fe_2O_3 is slightly higher than that in pure β-Fe_2O_3. $D_{I/C}$ and $D_{II/C}$ in the Cl-doped β-Fe_2O_3 are significantly higher than $D_{V/C}$ in the pure β-Fe_2O_3. These results indicate that the impurity band states introduced by Cl doping in β-Fe_2O_3 are extremely locative and have a higher D value, which is advantageous to suppress recombination between holes and electrons.[48, 49]

Table 4 Relative ratios in the VBM ($D_{V/C}$), B-I ($D_{I/C}$) and B-II ($D_{II/C}$) of 1.25% Cl-doped β-Fe_2O_3

		$D_{V/C}$	$D_{II/C}$	$D_{I/C}$
pure	Γ-H	3.554		
	Γ-N	3.651		
	Γ-P	3.635		
Cl doped	Γ-H	4.374	11.190	27.095
	Γ-N	4.430	21.637	16.173
	Γ-P	2.514	36.509	26.289

Conclusions

We proposed the strategy of halogen doping to narrow the band gap and suppress electron–hole recombination of β-Fe_2O_3 based on DFT computations, focusing on chlorine doping. Partial density of states and Bader analysis showed that one impurity band (B-I) consists of mostly residual electron transmission, and the other impurity band (B-II) is composed of the Fe–Cl bond. By increasing the Cl concentration, the interval between the impurity band and valence band disappears, which results in further narrowing of the energy gap. The STH efficiency increases from 20.6% in the pure β-Fe_2O_3 to 31.4% in the Cl-doped β-Fe_2O_3. Cl doping distorts the lattice structure and causes a larger effective mass around the VBM. The impurity levels are strongly locative owing to the properties of the Fe–Cl bond. The strong electron localization causes a relatively larger effective hole mass, which indicates strong suppression of electron–hole recombination.

This work provides a strategy for strengthening the absorption response over a long wavelength range and suppressing electron–hole recombination. Our results fill the gap in theoretical studies of halogen doping in β-Fe_2O_3 and pay the way

for studies of doping other elements. To further increase the photocatalytic performance of water splitting, codoping halogen and other atoms could be a good choice, which we will explore for the next step.

Conflicts of interest

There are no conflicts to declare.

Acknowledgements

This work was supported in China by National Natural Science Foundation of China (Nos. 22025202, 51972165), and Natural Science Foundation of Jiangsu Province of China (No. BK20202003), and in the USA by the Department of Energy (Grant DE-SC0023418). A portion of the calculations used the resources of the Compute and Data Environment for Science (CADES) at ORNL and of the National Energy Research Scientific Computing Centre, which are supported by the Office of Science of the U.S. DOE under Contract No. DE-AC05-00OR22750 and DE-AC02-05CH11231, respectively. Some of the work was performed at the Center for Nanophase Materials Sciences, a U.S. DOE Office of Science User Facility.

References

1. Y. Fang, Y. Zheng, T. Fang, Y. Chen, Y. Zhu, Q. Liang, H. Sheng, Z. Li, C. Chen and X. Wang, *Sci. China Chem.*, 2019, **63**, 149-181.
2. D. K. Lee, D. Lee, M. A. Lumley and K. S. Choi, *Chem. Soc. Rev.*, 2019, **48**, 2126-2157.
3. J. Feng, H. Huang, S. Yan, W. Luo, T. Yu, Z. Li and Z. Zou, *Nano Today*, 2020, **30**, 100830.
4. Y. Yang, S. Niu, D. Han, T. Liu, G. Wang and Y. Li, *Adv. Energy Mater.*, 2017, **7**, 1700555.
5. Y. Fang, Y. Zheng, T. Fang, Y. Chen, Y. Zhu, Q. Liang, H. Sheng, Z. Li, C. Chen and X. Wang, *Sci. China Chem.*, 2020, **63**, 149-181.
6. C. Ding, J. Shi, Z. Wang and C. Li, *ACS Catal.*, 2016, **7**, 675-688.
7. S. Feng, T. Wang, B. Liu, C. Hu, L. Li, Z. J. Zhao and J. Gong, *Angew Chem. Int. Ed. Engl.*, 2020, **59**, 2044-2048.
8. L. Pan, J. H. Kim, M. T. Mayer, M.-K. Son, A. Ummadisingu, J. S. Lee, A. Hagfeldt, J. Luo and M. Grätzel, *Nat. Catal.*, 2018, **1**, 412-420.
9. L. Lu and S. Yu, *J. Colloid Interf. Sci*, 2021, **593**, 116-124.
10. Y. Jing, X. Zhu, S. Maier and T. Heine, *Trends Chem.*, 2022, **4**, 792-806.
11. Y. Li, S. Wu, J. Zheng, Y.-K. Peng, D. Prabhakaran, R. A. Taylor and S. C. E. Tsang, *Mater. Today*, 2020, **41**, 34-43.
12. Q. Chen, G. Fan, H. Fu, Z. Li and Z. Zou, *Adv Phys-X*, 2018, **3**, 1487267.
13. Q. Liang, Y. Guo, N. Zhang, Q. Qian, Y. Hu, J. Hu, Z. Li and Z. Zou, *Sci. China Mater.*, 2018, **61**, 1297-1304.
14. Y. Zhang, N. Zhang, Y. Liu, Y. Chen, H. Huang, W. Wang, X. Xu, Y. Li, F. Fan, J. Ye, Z. Li and Z. Zou, *Nat. Commun.*, 2022, **13**, 2942.
15. J. H. Kim and J. S. Lee, *Adv. Mater.*, 2019, **31**, 1970146.
16. J. Fu, Z. Fan, M. Nakabayashi, H. Ju, N. Pastukhova, Y. Xiao, C. Feng, N. Shibata, K. Domen and Y. Li, *Nat. Commun.*, 2022, **13**, 729.
17. Y. Huang, Z. Guo, H. Liu, S. Zhang, P. Wang, J. Lu and Y. Tong, *Adv. Funct. Mater.*, 2019, **29**, 1903490.
18. N. Zhang, H. Zheng, Y. Guo, J. Feng, Z. Li and Z. Zou, *ACS Sustain. Chem. Eng.*, 2019, **7**, 10509-10515.
19. X. Xu, W. Wang, Y. Zhang, Y. Chen, H. Huang, T. Fang, Y. Li, Z. Li and Z. Zou, *Sci. Bull.*, 2022, **67**, 1458-1466.
20. C.-W. Lee, K.-W. Lee and J.-S. Lee, *Mater. Lett.*, 2008, **62**, 2664-2666.
21. Y. Li, N. Zhang, C. Liu, Y. Zhang, X. Xu, W. Wang, J. Feng, Z. Li and Z. Zou, *Chin. J. Catal.*, 2021, **42**, 1992-1998.
22. W. Wang, X. Wang, Y. Li, N. Zhang, M. Zhong, Z. Li and Z. Zou, *Phys. Chem. Chem. Phys.*, 2022, **24**, 6958-6963.
23. G. Kresse and J. Furthmüller, *Comput. Mater. Sci.*, 1996, **6**, 15-50.
24. J. P. Perdew, K. Burke and M. Ernzerhof, *Phys. Rev. Lett.*, 1996, **77**, 3865.
25. J. P. Perdew, A. Ruzsinszky, G. I. Csonka, O. A. Vydrov, G. E. Scuseria, L. A. Constantin, X. Zhou and K. Burke, *Phys. Rev. Lett.*, 2008, **100**, 136406.
26. S. L. Dudarev, G. A. Botton, S. Y. Savrasov, C. J. Humphreys and A. P. Sutton, *Phys. Rev. B*, 1998, **57**, 1505-1509.
27. V. I. Anisimov, J. Zaanen and O. K. Andersen, *Phys. Rev. B*, 1991, **44**, 943-954.
28. H. J. Monkhorst and J. D. Pack, *Phys. Rev. B*, 1976, **13**, 5188-5192.
29. N. Zhang, X. Wang, J. Feng, H. Huang, Y. Guo, Z. Li and Z. Zou, *Natl. Sci. Rev.*, 2020, **7**, 1059-1067.
30. S. Lany and A. Zunger, *Phys. Rev. B*, 2008, **78**, 235104.
31. Z. Li, W. Luo, M. Zhang, J. Feng and Z. Zou, *Energ. Environ. Sci.*, 2013, **6**, 347-370.
32. R. Zboril, M. Mashlan, D. Krausova and P. Pikal, *Hyperfine Interact.*, 1999, **120**, 497-501.
33. W. Setyawan and S. Curtarolo, *Comput. Mater. Sci.*, 2010, **49**, 299-312.
34. E. Pastor, M. Sachs, S. Selim, J. R. Durrant, A. A. Bakulin and A. Walsh, *Nat. Rev. Mater.*, 2022, **7**, 503-521.
35. N. Zhang, Y. Guo, X. Wang, S. Zhang, Z. Li and Z. Zou, *Dalton T.*, 2017, **46**, 10673-10677.
36. T. M. Henderson, J. Paier and G. E. Scuseria, *Phys. Status. Solidi. B*, 2011, **248**, 767-774.
37. J. Paier, R. Asahi, A. Nagoya and G. Kresse, *Phys. Rev. B*, 2009, **79**, 115126.
38. J. Paier, R. Hirschl, M. Marsman and G. Kresse, *J. Chem. Phys.*, 2005, **122**, 234102.
39. J. Guo, X. Liao, M.-H. Lee, G. Hyett, C.-C. Huang, D. W. Hewak, S. Mailis, W. Zhou and Z. Jiang, *Appl. Catal., B*, 2019, **243**, 502-512.
40. P. P. Filippatos, N. Kelaidis, M. Vasilopoulou, D. Davazoglou, N. N. Lathiotakis and A. Chroneos, *Sci Rep*, 2019, **9**, 19970.
41. W. Li, *physica status solidi (RRL) - Rapid Research Letters*, 2015, **9**, 10-27.
42. W. Wang, P. J. Strohbeen, D. Lee, C. Zhou, J. K. Kawasaki, K.-S. Choi, M. Liu and G. Galli, *Chem. Mater.*, 2020, **32**, 2899-2909.
43. G. C. Vásquez, S. Z. Karazhanov, D. Maestre, A. Cremades, J. Piqueras and S. E. Foss, *Phys. Rev. B*, 2016, **94**, 235209.
44. E. Sanville, S. D. Kenny, R. Smith and G. Henkelman, *J. Comput. Chem.*, 2007, **28**, 899-908.

45. W. Tang, E. Sanville and G. Henkelman, *J. Phys-Condens. Mat.*, 2009, **21**, 084204.
46. H. Zhang, L. Liu and Z. Zhou, *RSC Adv.*, 2012, **2**, 9224-9229.
47. H. Zhang, L. Liu and Z. Zhou, *Phys. Chem. Chem. Phys.*, 2012, **14**, 1286-1292.
48. X. Liu and K. Sohlberg, *Comput. Mater. Sci.*, 2016, **123**, 1-7.
49. M. A. Green, *J. Appl. Phys.*, 1990, **67**, 2944-2954.